PCCP

ROYAL SOCIETY OF CHEMISTRY

PAPER

View Article Online
View Journal | View Issue

Cite this: *Phys. Chem. Chem. Phys.*, 2020, **22**, 3499

Citrate combustion synthesized Al-doped $CaCu_3Ti_4O_{12}$ quadruple perovskite: synthesis, characterization and multifunctional properties

Kamalesh Pal,[a] Arka Dey,[bc] Rajkumar Jana,[b] Partha P. Ray,[b] Parthasarathi Bera,[d] Lalit Kumar,[e] Tapas Kumar Mandal,[e] Paritosh Mohanty,[e] Md. Motin Seikh *[f] and Arup Gayen *[a]

Received 10th September 2019,
Accepted 9th January 2020

DOI: 10.1039/c9cp05005a

rsc.li/pccp

The facile synthesis of the Al-doped $CaCu_3Ti_4O_{12}$ quadruple perovskite, a well-known and vastly studied material for various technological applications, using the modified citrate combustion route along with structural, microstructural, and X-ray photoelectron spectroscopic (XPS) characterization and magnetic, dielectric and electrical properties has been investigated and reported here. The possible applications of the material as a Schottky barrier diode (SBD) in optoelectronic devices and as a catalyst in methanol steam reforming (MSR) reaction for hydrogen generation, hitherto unreported in the open literature, have also been explored. The compound is crystallized in the cubic body centered $Im\bar{3}$ space group and the particle size is found to be in nanodimension with rather narrow size distribution. The enhanced resistivity could be attributed to the grain boundary effect, and consequently, it exhibits better performance as a SBD compared to the undoped sample. Desired cationic composition with expected valence states within the probe range is confirmed by XPS analysis. A better catalytic activity towards MSR is noticed for the Al-doped $CaCu_3Ti_4O_{12}$ compared to the undoped composition. These new findings, namely MSR activity and applicability in the Schottky device, have highlighted further the multifunctional nature of the material in energy related issues and would thus be of interest to the materials community searching for functional materials.

1. Introduction

Functional materials with large dielectric values can have potential application in energy storage devices such as capacitors/supercapacitors and memory-based devices. In this regard, the quadruple perovskite $CaCu_3Ti_4O_{12}$, abbreviated as CCTO, is considered as an important material having a high dielectric constant (10^4–10^5) at room temperature.[1–4] This material has attracted large attention after the discovery of giant dielectric constant by Subramanian *et al.* in 2000.[1,2] Interestingly, unlike other members of this family of oxides, which require high pressure to synthesize, CCTO has been reported to be synthesized at ambient pressure in the 1970s by Deschanvres *et al.*[5] Extensive investigations have been carried out to explore the origin of such high dielectric value of CCTO. Though the most popular approach employed to explain the high dielectric value is internal barrier layer capacitance (IBLC) theory, the exact mechanism is yet to be resolved.[6–9] In addition to the giant dielectric constant, CCTO also possesses interesting magnetic, electric and catalytic properties. CCTO also exhibits antiferromagnetic ordering at ~34 K, whereas the isostructural $CaCu_3Mn_4O_{12}$ and $ThCu_3Mn_4O_{12}$ are ferrimagnetic at Curie temperature (T_C) at 355 and 430 K, respectively, which are much higher than room temperature.[10,11] Other fascinating properties observed in CCTO are the non-Ohmic current–voltage (I–V) characteristics credited to the intrinsic electrostatic barrier at the grain boundary and optical responses.[3,12–15] The strong nonlinear I–V characteristics of CCTO have been discovered by Chung *et al.* with a nonlinear coefficient of about 900, which is very high in comparison to that of the conventional ZnO varistor.[12,16] Regarding catalytic activity, the presence of well-known oxides of copper and titanium could have made the material

[a] *Department of Chemistry, Jadavpur University, Kolkata 700032, India. E-mail: agayenju@yahoo.com, arup.gayen@jadavpuruniversity.in; Fax: +91-33-2414-6223; Tel: +91-33-2457-2767*
[b] *Department of Physics, Jadavpur University, Kolkata 700032, India*
[c] *Department of Condensed Matter Physics and Material Sciences, S. N. Bose National Centre for Basic Sciences, Kolkata 700106, India*
[d] *Surface Engineering Division, CSIR – National Aerospace Laboratories, Bengaluru 560017, India*
[e] *Department of Chemistry and Centre of Nanotechnology, Indian Institute of Technology Roorkee, Roorkee 247667, India*
[f] *Department of Chemistry, Visva-Bharati, Santiniketan 731235, India. E-mail: mdmotin.seikh@visva-bharati.ac.in; Fax: +91-3463-262672; Tel: +91-9933052194*

suitable for application in the field of catalysis. However, a few studies have been performed to explore the catalytic effect of CCTO which have specifically highlighted the material as a photocatalyst.[15,17] Till date, except our recent report, the activity of this material in heterogeneous catalysis has remained unexplored.[18]

Numerous synthetic methods have been followed by the researchers to improve the dielectric, electric, magnetic and electromagnetic behavior of CCTO.[18–26] Among the various methods solid state synthesis is the most common and widely used synthetic method, although it requires a very high calcination temperature with a long sintering time.[19,20] Again the citrate combustion route is one of the simple synthetic methods, which requires comparatively low calcination temperature as well as sintering time and the microstructure can be easily tuned. Several studies have also been performed to improve the aforesaid behaviour of the material by introducing various ions at Ca, Cu and Ti-sites. In this regard, Al-doping at the Ti-site has appeared to be advantageous in terms of reduction in dielectric loss without compromising the high dielectric constant.[27–30] This type of behavior in Al-doped CCTO has been attributed to the enhanced grain boundary resistivity and the corresponding activation energy in the grain boundary.[27,29,31]

In our previous work, we have reported the synthesis of pure CCTO and Mn-doped CCTO (doped at both Cu and Ti-sites) by a modified citrate combustion method at low calcination temperature. The dielectric and magnetic behaviour of the pure CCTO and the effect of Mn-doping when compared with the pristine material have been discussed.[18] The doped material shows a small increase in the dielectric values and a remarkable change in the magnetic behavior with respect to undoped CCTO. Our recent studies have explored the catalytic activity of CCTO and Mn-doped CCTO in methanol steam reforming (MSR) and CO oxidation reaction. Mn-doping in this regard has been found to be beneficial compared to the pristine material. Bearing in mind such improved properties in substituted CCTO, we have attempted to further explore the Al-doped system.

Here, we report a thorough investigation of the synthesis, microstructural analysis (using transmission electron microscopy (TEM) and X-ray photoelectron spectroscopy (XPS)), redox properties by temperature programmed reduction (TPR), and magnetic and dielectric properties of Al-doped CCTO along with the possible applications as a catalyst in MSR reaction and as a Schottky barrier diode (SBD) in optoelectronic devices. Interestingly, the Al-doped sample exhibits an improved catalytic activity towards MSR compared to the pristine CCTO and a better SBD performance with respect to undoped and Mn-doped CCTO.

2. Experimental details

2.1. Materials

Precursor materials such as $Ca(NO_3)_2{\cdot}4H_2O$ (>99%), $Cu(NO_3)_2{\cdot}3H_2O$ (>99%) and $Al(NO_3)_3{\cdot}9H_2O$ (>99%) were obtained from Merck India. Citric acid (CA, 99%) and acetylacetone (>98%) were purchased from Merck India, and titanium tetraisopropoxide (TTIP, 97%) was procured from Sigma-Aldrich.

2.2. Synthesis

Nanosized Al-doped calcium copper titanate was synthesized in two steps: first, a modified citrate combustion method was used to prepare the oxide precursor as reported in our previous work and this was followed by its calcination at higher temperature in the second step to obtain the target quadruple perovskite.[18] In brief, stoichiometric amounts of the respective metal nitrate salts, $Ca(NO_3)_2{\cdot}4H_2O$, $Cu(NO_3)_2{\cdot}3H_2O$ and $Al(NO_3)_3{\cdot}9H_2O$, were at first dissolved in deionized (~100 mL) water followed by the addition of citric acid (two times with respect to the total mole of metal) as a fuel. Acetylacetone and titanium tetraisopropoxide were mixed separately in 1:1 molar ratio. Thus the total molar ratio of the metals was maintained at Ca:Cu:Ti:Al = 1:2.5:3.5:1. A green colored clear solution was obtained by mixing these two solutions. The pH of the solution was measured to be ~1 and the solution was stirred overnight to form a gel without regulating the pH. The gel was strongly heated (~200 °C) to obtain the reaction crude/precursor material, which was calcined at 800 °C for 2 h with a heating rate of 10 °C min^{-1} to get the final perovskite. It is to be noted that calcination at a lower temperature of 680 °C was also checked which was found to be insufficient for the desired phase formation. The pristine oxide CCTO′ was also prepared similarly for comparison, wherever required. Oxides of copper, titanium (primarily rutile) and aluminium (mainly α) were also synthesized following the same method, while calcium oxide was prepared by the coprecipitation method to compare the redox behavior of these individual oxides with the quadruple perovskite. Higher ordered perovskite materials used in the present investigation are $CaCu_3Ti_4O_{12}$ and Al-doped $CaCu_3Ti_4O_{12}$, *i.e.*, $CaCu_{2.5}Ti_{3.5}AlO_{12}$, which are henceforth designated as CCTO′ and ACCTO1′, respectively.

2.3. Characterization

2.3.1. Phase analysis. The powder XRD data were collected on a Bruker D8 Advance X-ray diffractometer using CuKα radiation (λ = 1.5418 Å) operating at 40 kV and 40 mA. The diffraction patterns were recorded using a Lynxeye detector (1D mode) at a scan time of 2 s per step and analyzed by the ICDD (International Centre for Diffraction Data) database for phase identification. Average sizes of the particles were calculated from the full width at half maximum (FWHM) of the diffraction peaks using Scherrer's equation. Rietveld refinement was done with the help of the FullProf-fp2k program to know the structural information of the material.

2.3.2. Microstructural analysis. The transmission electron microscopy (TEM) study was done on a JEOL JEM 3200FS operated at an accelerating voltage of 300 kV. In each measurement, a small quantity of the powder was mixed with methanol, ultrasonicated for a few minutes and a drop of the dispersion formed so was transferred to a holey carbon film deposited on a Cu grid of 300 mesh size. Suitable regions in the grid were selected for microscopy and selected area electron diffraction (SAED).

2.3.3. XPS analysis. The XPS analysis was carried out using a PHI-5000 VersaProbe III XPS spectrophotometer (ULVAC-PHI Inc.). The measurement was performed using monochromatic

AlKα radiation (1486.6 eV) as an X-ray source operated at 150 W (15 kV and 10 mA). The binding energy for individual elements was scaled with reference to the C 1s peak at 284.8 eV. The survey spectrum was recorded with a pass energy and step increment of 70 and 0.5 eV, respectively, and individual core level spectra were obtained with a pass energy and step increment of 40 and 0.05 eV, respectively. The analysis was performed by mounting the specimen in a pellet form with a dimension of 9 mm and keeping it overnight in the sample introduction chamber under ultra-high vacuum (5.0×10^{-6} mbar). The next day, the sample was transferred to the analysis chamber with a vacuum of 5.0×10^{-9} mbar and the XPS data were recorded. The PeakFit v4.11 program was employed for the curve-fitting of the Cu 2p, Cu 3p–Al 2p and O 1s core level spectra into several components with Gaussian peaks after linear background subtraction. Peak positions, spin–orbit splitting, doublet intensity ratios, and FWHM were fixed as given in the literature.

2.3.4. TPR analysis. The temperature programmed reduction analysis was performed using a Quantachrome ChemStar_TPX chemisorption analyzer using 50 mg of powdered material, taken in a U-shaped quartz reactor. Prior to introducing the reduction atmosphere, the sample was heated to 200 °C with a heating rate of 10° min^{-1} and held for 30 min. The complete pre-treatment step was performed in the presence of a stream of He with a flow rate of 35 mL min^{-1}. The reactive gas stream of 10% (v/v) H_2/Ar with a flow rate of 50 mL min^{-1} was then introduced and the H_2 consumption was continuously monitored using a thermal conductivity detector (TCD) from room temperature to 1000 °C with a heating rate of 10° min^{-1}.

2.4. Properties

2.4.1. Magnetic studies. The dc magnetization measurements were performed using a Mini Vibrating Sample Magnetometer (VSM) with a pulse Cryocooler (Cryogenics Ltd, UK). The temperature dependent magnetization measurements were performed using the zero field-cooled (ZFC) and field-cooled (FC) protocols at 500 Oe applied field in the temperature range of 5 K to 300 K. The isothermal magnetization measurements were carried out at different temperatures up to an applied field of ±3 T. All the magnetic measurements were performed on compact powder samples.

2.4.2. Dielectric studies. The dielectric properties were studied by impedance analysis to evaluate capacitance (C), impedance (Z) and phase angle (θ) of the sample as a function of frequency (40 Hz–11 MHz) at room temperature in an Agilent make precision 4294A LCR meter. The measurements were performed on disc shaped circular pellets of 1.5 mm thickness and 6 mm diameter having a density of ~1.53 g cm^{-3}, obtained by cold pressing the powder samples at 6 ton of pressure for 10 min under a hydraulic press. High purity ultrafine silver paste was coated on the opposite surfaces of the pellets for electrical connection.

2.4.3. Fabrication of the Schottky device. The thin film Schottky device was fabricated in a sandwich like ITO/oxide/Al (oxide = CCTO′ and ACCTO1′, ITO: indium tin oxide) configuration. At first, the ITO coated glass substrate was cleaned sequentially with soap solution, acetone, ethanol, and distilled water in an ultrasonic bath. A stable dispersion of the powdered perovskite material in acetone medium was then made in the desired proportion (20 mg mL^{-1}). The material was deposited as a thin film on the ITO coated glass by the spin coating technique at 1200 rpm for 2 min with the help of the SCU 2700 spin coating unit and then dried overnight under vacuum at 100 °C to ensure complete evaporation of the solvent. The thickness of the thin film developed so was measured by using a surface profiler to be 1 μm. Aluminium was chosen as the rectifier metal contact and deposited on the films by the thermal evaporation technique by using a vacuum coating unit (12A4D of HINDHIVAC) under a base pressure of 1.33×10^{-6} mbar to make a metal–semiconductor junction. The effective diode area of the film was maintained at 7.065×10^{-6} m^2 by using a shadow mask.

2.4.4. Electrical studies. To analyse the electrical properties of the fabricated device, we measured the current at the corresponding applied bias voltage sequentially within the limit of ±2 V, both under dark and under 1.5G AM radiation. The I–V measurement was carried out using a Keithley 2635B source-meter interfaced with a computer by the two-probe technique.

2.4.5. MSR studies. The MSR experiment was performed in a fixed-bed down flow quartz reactor in the temperature range of 130–370 °C at atmospheric pressure following our earlier reported experimental studies.[18] In an experiment, 0.1 g of sample of 85–100 mesh size was packed inside the reactor on a quartz wool bed and placed vertically inside a tube furnace. A premixed liquid mixture of water (Millipore) and methanol (Spectrochem, HPLC grade) corresponding to a steam to carbon (S/C) molar ratio of 1.1 was injected by using a KD100 syringe pump (Cole Parmer) at a rate of 0.5 mL h^{-1}. The gas hourly space velocity (GHSV) was kept constant at 33 000 h^{-1} using N_2 as the carrier as well as the internal standard with a flow rate of 24 mL min^{-1}. The noncondensable products were analyzed by using an Agilent 7890A gas chromatograph equipped with polar Porapak Q and molecular sieve 5 Å columns, a thermal conductivity detector (TCD) and a flame ionization detector (FID). Due to the absence of CH_3OH in the GC, the conversion was calculated by using a carbon balance method.

3. Results and discussion

3.1. XRD studies

Fig. 1 shows the Rietveld refined powder XRD patterns of ACCTO1′ and CCTO′ which confirm the formation of the quadruple perovskite phase with traces of additional reflection. The diffraction patterns are completely indexed with the majority peaks akin to CCTO using the cubic space group ($Im\bar{3}$) (ICDD PDF # 75-2188) along with a trace amount (<0.5%) of $CuAl_2O_4$ (ICDD PDF # 73-1958) in ACCTO1′ and <2% of CuO impurity phase in CCTO′.

Thus Al-doping enhances the phase purity of the quadruple perovskite and is associated with a near absence of CuO in the ACCTO1′ sample. No impurity of $CaTiO_3$, as commonly reported in earlier literature, is detected for both these materials.[19,32] The obtained cell and other refined parameters from Rietveld

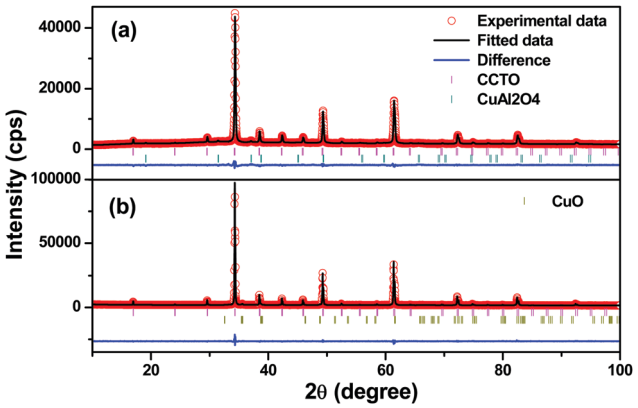

Fig. 1 The powder X-ray diffraction patterns with Rietveld refinement for (a) ACCTO1′ and (b) CCTO′. The open red circles, the black line, the bottom blue line and the vertical bars represent the experimental data, calculated pattern, difference curve and the Bragg positions, respectively. The magenta, dark cyan and dark yellow vertical bars show the Bragg positions for CCTO, $CuAl_2O_4$ and CuO, respectively.

refinement of the patterns are listed in Table 1. The bond lengths and bond angles are in excellent agreement with the reported values.[33] The average crystallite size calculated from FWHM of the (220) diffraction line using Scherrer's formula is found to be ~67 nm for CCTO′ which decreases to ~48 nm when doped with aluminium in ACCTO1′.[34] Since $Al(NO_3)_3{\cdot}9H_2O$ is taken as the precursor of Al, it is expected to form Al_2O_3 after decomposition due to its high thermodynamic stability. Again, Al_2O_3 is a well-known refractory material and it is expected to react rather slowly. This could be at the origin of smaller particle size of the Al-doped sample.

The crystallite size ($D = K\lambda/\beta{\cdot}\cos\theta$), lattice strain ($\varepsilon = \beta/4{\cdot}\tan\theta$) and dislocation density ($\delta = 1/D$) calculated from the powder diffraction patterns of quadruple perovskites CCTO′ and ACCTO1′ are summarized in Table 1.[35,36] In the equation, β is FWHM in radian, λ is the wavelength of the incident X-ray and θ denotes Bragg's angle. It is observed that the doped material shows comparatively lower crystallite size than that of the undoped material which also supports our structural findings obtained from Rietveld refinement. On the other hand, increased δ and ε values for the doped sample indicate reduction in crystalline quality.

3.2. Microstructural studies

Low magnification TEM and HRTEM images of ACCTO1′ and CCTO′ are shown in Fig. 2. The TEM images show that the particles are of irregular shape having sizes in the range of 20–120 nm in ACCTO1′, while the irregular particles are larger in size in the range of 50–500 nm in CCTO′. The HRTEM images of both the samples depict clear lattice fringes of 0.402 and 0.369 nm corresponding to the (200) plane of ACCTO1′ and CCTO′, respectively. These values match well with the results obtained from the XRD studies. Indexing of the SAED patterns (Fig. 2(c and f)) for both the samples further supports the XRD data.

3.3. XPS studies

XPS is one of the important tools to study the surface composition and elemental oxidation states of materials. In several cases, it can provide information about metal binding energy change because of the different coordination environment with oxygen ions.[37] In the CCTO quadrupole perovskite structure, Ti^{4+} ions are in octahedral coordination and Cu^{2+} ions are in four coordinated square planar coordination, which is comparable to the flattened tetrahedral coordination. The dopant Al^{3+} ions are unlikely to occupy square planar coordination, but they can be in octahedral coordination. In the Al-doped sample, there are minor impurities of $CuAl_2O_4$ and CuO as evident from XRD analysis. It is worth noting that $CuAl_2O_4$ is basically a mixed spinel, *i.e.* Cu^{2+} and Al^{3+} are randomly distributed in both the tetrahedral and octahedral sites of the spinel structure. Again, unlike in CCTO, Cu^{2+} in CuO is in octahedral coordination. Therefore, a careful XPS analysis of ACCTO1′ has been carried out keeping in mind all the above factors. The XPS survey spectrum and different core-level spectra of Al-doped CCTO are shown in Fig. 3. The survey spectrum (see Fig. 3(a)) indicates the presence of the desired elements such as Ca, Cu, Ti, Al and O in the oxide. The envelope of the Ca 2p core level spectrum is observed to be broad in nature indicating that different Ca species are present on the surface which is curve-fitted into component species. The Ca $2p_{3/2,1/2}$ spin–orbit doublet centred at 346.3 eV and 349.7 eV confirms the presence of Ca in +2 oxidation state (see Fig. 3(b)).[38] Binding energy peaks observed at 347.3 and 350.8 eV are attributed to other oxidized Ca species

Table 1 Summary of structural parameters of ACCTO1′ and CCTO′ (S.G. $Im\bar{3}$)

Sample	Cell parameter (Å)	R_B (%)	R_F (%)	χ^2	FWHM (β_{220}°)	2θ (°)	Crystallite size D (nm)	Dislocation density δ ($\times10^{-3}$)	Micro strain ε ($\times10^{-3}$)
ACCTO1′	7.393 (±2)	3.01	5.12	2.37	0.172	34.30	48	20.8	2.43
CCTO′	8.046 (±2)	4.06	5.51	2.91	0.126	34.26	67	14.9	1.78

Atom	Ox.	Wyck.	Occ.	X	y	z	U
Ca	+2	2a	1	0	0	0	0.0058
Cu	+2	6b	1	0	1/2	1/2	0.0045
Ti/Al	+4	8c	1	$\frac{1}{4}$	1/4	1/4	0.0053
O	−2	24g	1	0.30410	0.17990	0	0.0089

Bond length (Å)			Bond angle (°)		
d_{Ca-O}	d_{Cu-O}	$d_{Ti/Al-O}$	∠Ti–O–Ti	∠O–Cu–O	∠O–Ti–O
2.610	1.965	1.959	140.99	85.12	89.83

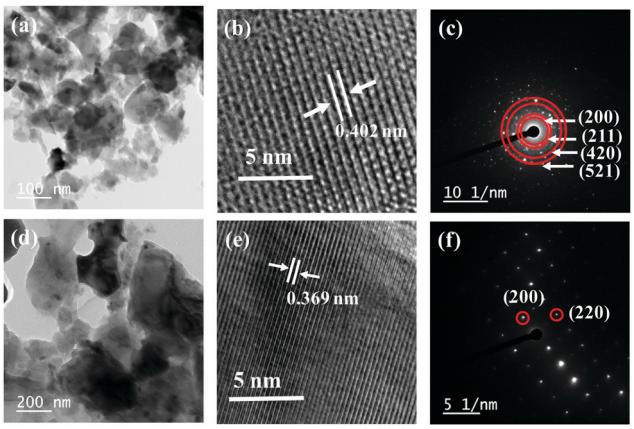

Fig. 2 Low magnification TEM, HRTEM and SAED patterns of ACCTO1′ (a–c) and CCTO′ (d–f).

such as $CaCO_3$ formed during the preparation. The observed Ti $2p_{3/2,1/2}$ doublet at 457.9 eV and 463.7 eV corresponds to Ti^{4+} (see Fig. 3(c)).[39] The Cu 2p core level spectrum of ACCTO is broad indicating the presence of different Cu species which is decomposed into different component peaks by curve-fitting. Accordingly, Cu $2p_{3/2,1/2}$ peaks at 933.7 and 953.6 eV with characteristic satellite peaks and a spin–orbit separation of 19.9 eV are attributed to Cu^{2+} species present in the ACCTO material (see Fig. 3(d)). Satellite peaks are special features of oxidized transition metals such as Fe, Co, Ni and Cu. It is well established that an additional excitation of a second electron takes place during the creation of a hole in a core level by photoelectron emission. The sudden hole creation in the Cu $2p^6$ filled orbital from the Cu^{2+} ion present in the catalyst forms the Cu^{3+} ion which is unstable. Therefore, an electron transfer from the O 2p level to Cu 3d level occurs resulting in satellite peaks in the Cu 2p core level spectrum as observed in the figure. In addition, weak component $2p_{3/2,1/2}$ peaks at 935.6, 955.2 and 932.8, 952.3 eV are also observed in the Cu 2p spectrum. It has been reported in the literature that Cu 2p binding energy decreases when changing from tetrahedral to octahedral sites corresponding to an increase in Cu coordination number with oxygen ions.[40,41] Therefore, Cu $2p_{3/2,1/2}$ peaks at 933.7 and 953.6 eV are assigned to Cu in octahedral sites indicating the presence of CuO. As the tetrahedral coordination environment is comparable to the square planar environment, Cu $2p_{3/2,1/2}$ peaks at 935.2 and 955.2 eV stand for Cu in square planar sites in the ACCTO structure. Lower binding energy peaks are related to Cu^{+} species present in the material. It is to be noted that the concentration of the CuO species is more compared to square planar Cu species on the surface of the material which is different from the respective bulk concentrations. The existence of CuO within the material can be further understood by the ratio of the intensity of the shake-up satellite peak to the intensity of the main Cu $2p_{3/2}$ peak ($I_{satellite}/I_{main\ peak}$). If only CuO species is present in the catalysts then the ratio should be 0.55.[42] However, the observed value in the present material is 0.53 which is closer to the CuO value. Similar results are also obtained while analyzing the Cu 3p–Al 2p core level spectrum which is shown in Fig. 3(e) as they overlap. The broad spectrum indicates the presence of different Cu and Al species. The higher binding energy region of the spectrum is related to the Cu 3p core level and 3p peaks observed at 76.2 and 78.4 eV are assigned to octahedral and square planar Cu in the ACCTO material.[41] The lower binding energy region is associated with the Al 2p core level that shows 2p peaks centred at 73.5 and 74.3 eV. Several XPS studies have been attempted to distinguish the coordination environment of Al in different Al based compounds. Al 2p binding energy increases with an increase in the ratio of octahedral to tetrahedral Al and the binding energy value of octahedral and tetrahedral Al depends on the ionic character of the Al–O bond which is influenced by the surrounding environment.[41,43,44] Within this context, the observed Al 2p core level peaks at 73.5 and 74.3 eV in ACCTO are attributed to tetrahedral and octahedral Al, respectively. The O 1s core level spectrum of the material has also been recorded. The broad spectral envelope of the O 1s core level indicates the presence of different oxygen species in the catalysts that can be related to different metal–oxygen bonds such as Ca–O, Cu–O, Ti–O, and Al–O present in the material. In this regard, the spectrum is resolved into component peaks by curve fitting which is displayed in Fig. 3(f). The decomposed peak at 528.6 eV is attributed to the oxide ion (O^{2-}) of the Ca–O bond and the peaks around 529.9 and 531.5 eV correspond to the oxide ion (O^{2-}) of Cu–O/Ti–O and Al–O bonds, respectively.[45] It is well established that binding energies determined by XPS for the core electrons of an atom depend on the chemical state of the atom in the particular compound. Generally, an increase in the negative charge on the ionized atom leads to the lowering of the core level binding energies. In the present study, a large difference in O 1s core level binding energies among Ca–O, Cu–O/Ti–O and Al–O bonds indicates the highest electron population in the O atom in the Ca–O bond followed by Cu–O/Ti–O and Al–O bonds that depends on the number of oxygen coordination and electronegativity. Alkaline earth metals like Ca have low electronegativity and hence there is a trend to increase electron density on surrounding oxygen atoms in the Ca–O bond. In a theoretical work of Dupin and co-authors, the net charge on oxygen is observed to be more in alkaline earth metal oxides compared to transition metal oxides which leads to an increase in electron density on the O atom in alkaline earth metal oxides.[45]

3.4. Magnetic properties

The FC and ZFC curves mostly overlay on each other in the entire temperature range of measurement (see Fig. 4a and b). The magnetization *vs.* temperature plot indicates the onset of an antiferromagnetic transition around 25 K. This result suggests that non-magnetic Al-loading in CCTO′ does not alter the magnetic behavior as evidenced from the similar magnetization curve of the pristine sample (Fig. 4(b)). This observation is in agreement with the reported values of CCTO′ [18,46–50] and it is significantly different from the magnetic ion doping in CCTO′.[18,51,52] The low temperature antiferromagnetic behavior of ACCTO1′ is evidenced from the linear response of magnetization with applied field at 5 K (Fig. 4(c)). The linear field dependence of magnetization at 300 K (Fig. 4(c)) is due to the paramagnetic

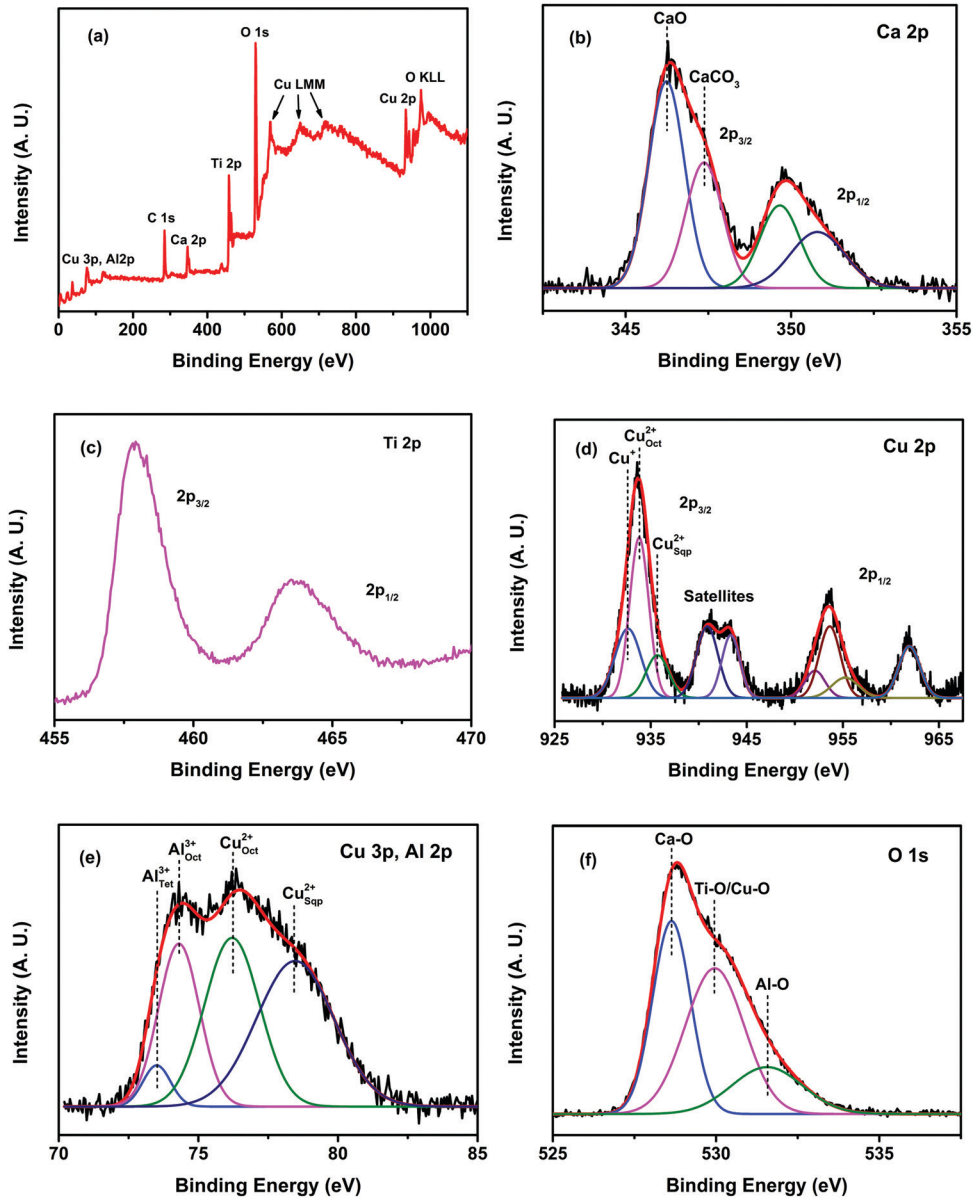

Fig. 3 XPS of ACCTO1′: (a) survey spectrum, and (b) Ca 2p, (c) Ti 2p, (d) Cu 2p, (e) Cu 3p, Al 2p and (f) O 1s core level spectra.

behavior of the sample. This field dependence of ACCTO1′ is very similar to the pristine sample (Fig. 4(b)). The observed paramagnetic moment calculated from the high temperature slope (temperature range 125–300 K) of the field cooled (FC) inverse susceptibility data using the Curie–Weiss law is 3.95 μ_B f.u.$^{-1}$ (see the inset in Fig. 4(a)) and the associated Weiss constant (Θ_{CW}) is −139 K. This Weiss constant is slightly higher than that of the pristine sample.[46] The effective magnetic moment is slightly higher than the calculated spin only moment of 3.23 μ_B f.u.$^{-1}$. However, the observed value of CCTO′ is in very good agreement with the calculated value of 3.54 μ_B f.u.$^{-1}$ (inset in Fig. 4(b)). One should also notice the high Θ_{CW} (−139 K) value of ACCTO1′ compared to that of CCTO′ (−26.5 K). This indicates that Al-doping tends the magnetization towards frustration as the frustration parameter $f = \Theta_{CW}/T_N > 5$. It is worth mentioning that for the calculation of spin moment the effective g-value of square planar Cu^{2+} is taken to be 2.36 as reported in the literature.[46,53] Thus, the magnetic measurements indicate that unlike the substitution by magnetic ions the diamagnetic substitution does not hamper the magnetic super-exchange interaction between Cu^{2+} in the A-site largely.[49–51]

3.5. Dielectric properties

Fig. 5(a) shows the impedance loss spectra of ACCTO1′. Formation of a peak at higher frequencies signifies the presence of a relaxation process in the grain and grain boundary region of the sample. The asymmetric nature of the Z'' peak suggests the presence of an electrical process in the material and its peak width indicates the distribution of relaxation time.[54,55] The Z'' spectrum becomes saturated in the high frequency region which may be

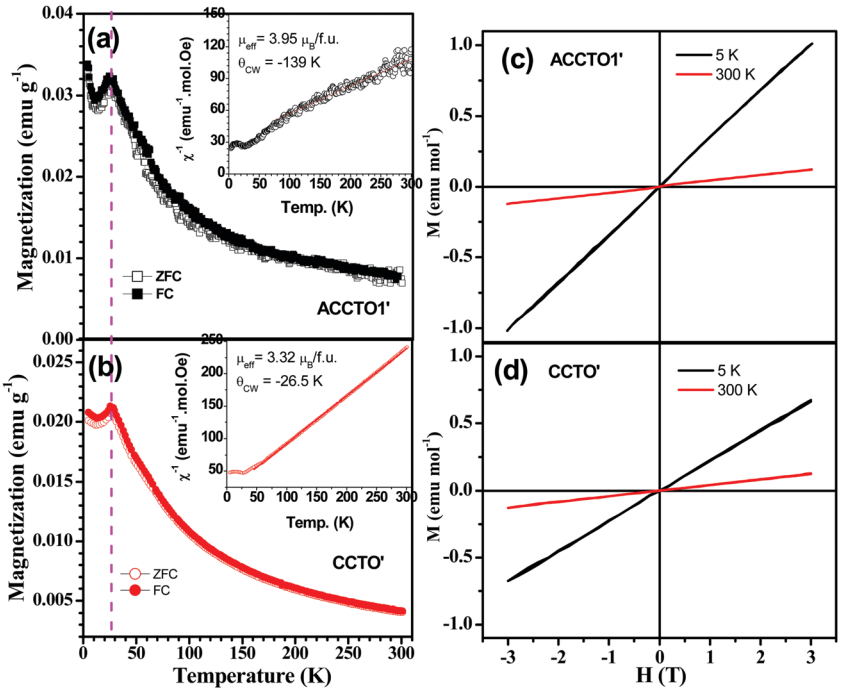

Fig. 4 (a) ZFC–FC magnetization of ACCTO1′. The inset shows the inverse susceptibility plot of FC data along with the Curie–Weiss plot (red solid line), (b) ZFC–FC data of undoped CCTO′, and (c) and (d) show the field dependent magnetization of ACCTO1′ and CCTO′, respectively at 5 K and 300 K.

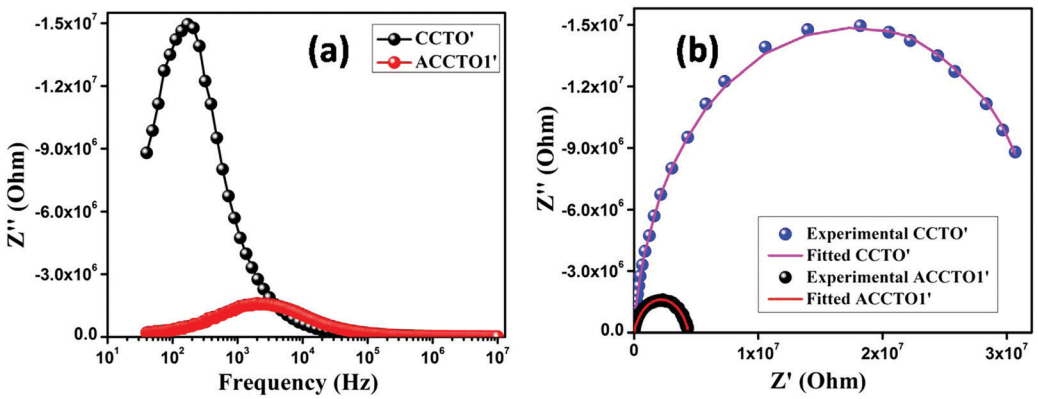

Fig. 5 (a) Angular frequency dependent Z'' plot and (b) complex impedance plot for CCTO′ and ACCTO1′ at room temperature.

due to the space charge accumulation in the material.[56] The plot displays a peak at ω_{max} which is inversely related to the relaxation time ($\tau_n = 1/\omega_{max}$) of charge carriers that has been calculated to be 7.93×10^{-5} s and 9.33×10^{-4} s for ACCTO1′ and CCTO′, respectively.[57]

Fig. 5(b) shows the complex plane impedance plot, *i.e.* the Nyquist plot. The bulk resistance R_b (dc resistance) of the sample at the electrode/composite interface obtained from the radius of the semicircle has been calculated to be 4.4×10^6 Ω and 3.7×10^7 Ω for ACCTO1′ and CCTO′, respectively.[58]

Fig. 6(a) represents the real part of complex permittivity of the sample as a function of frequency which decreases with the increase of frequency and approaches a constant value due to the dipole polarization processes. At lower frequencies, the movement of charge carriers trapped at the interfacial region is influenced by the inhomogeneous dielectric structure. On the other hand, at higher frequencies, the charge carriers are no longer able to rotate sufficiently, and their oscillation begins to lag behind the applied field resulting in a decrease of dielectric permittivity.[59] The dominant mechanism contributing to the dielectric constant at higher frequency is the hopping mechanism associated with the interstices. The frequency of hopping between ions cannot follow the frequency of the applied field and hence it lags behind contributing to the reduction of dielectric constant at higher frequency.[60]

The existence of typical Maxwell–Wagner (MW) relaxation is observed by the inflexion in the real part of dielectric response, which corresponds to the tan δ *vs.* frequency plot (see Fig. 6(b)).

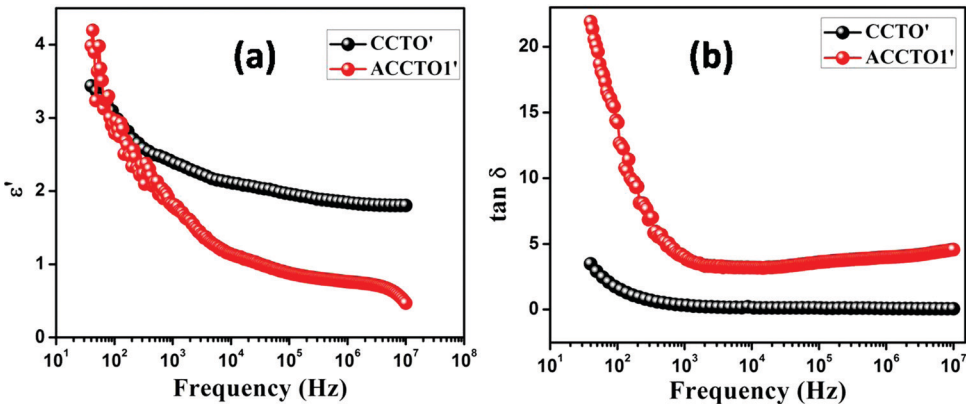

Fig. 6 Frequency dependence of the (a) real part of complex permittivity and (b) dielectric loss for CCTO′ and ACCTO1′.

The dielectric loss decreases with the increase in frequency and attains a minimum value which is a general feature of polar dielectric materials.[61] Besides the decrease of ε', a reduction of $\tan\delta$ in the high frequency region ($>10^3$ Hz) can be related to the absence of the relaxation process in this frequency region. The variation of loss tangent with frequency can be described by the space charge polarization based on the Wagner and Maxwell model.[62] In the lower frequency region, the dielectric loss is maximum because the carrier transport through unpolarized material is controlled only by the applied field. On the other hand, in the higher frequency region, the carrier transport is governed by the field generated due to the polarized dielectric medium under the applied field.

The ac conductivity pattern of the sample shows a frequency independent flat terrain in the low frequency region (see Fig. 7(a)) and exhibits dispersion at higher frequencies which occurs due to the polarization effect of the medium.[63] The dc conductivity obtained from the extrapolation of the conductivity curve to the y-axis is found to be 2.04×10^{-6} S m^{-1} and 2.66×10^{-7} S m^{-1} for ACCTO1′ and CCTO′, respectively, which is caused by the long range translational motion of the charge carriers. According to the Jump Relaxation Model (JRM), in the low-frequency region, the conductivity is associated with the successive and successful hopping movement of charged particles to the vacant sites of their neighbourhood due to the availability of a long time period resulting in a long range translational motion of the charge carrier to the dc conductivity.[64] The frequency-dependent conduction could be attributed to localized orientation hopping aided by the polaron mechanism.[65] In the low frequency region, the electric field cannot perturb the hopping conduction mechanism of charged particles and hence the conductance is approximately equal to the dc value.[66]

Fig. 7(b) presents the variation of capacitance with frequency at a constant bias potential. The room temperature capacitance shows frequency dependency at relatively low values. So, the material pellet consisting of dipoles behaves like a capacitor's dielectric medium.[67] The dielectric constant estimated from the saturation level is ~2401 and 406 for ACCTO1′ and CCTO′, respectively. The high capacitance at lower frequencies may be attributed to the significant polarization of charge carriers. The dipoles cannot orient themselves at higher frequencies and hence the capacitance decreases.

3.6. Electrical properties

Fig. 8 presents the current *vs.* voltage (I–V) graph of ACCTO1′ and CCTO′ under dark and light conditions. The curve exhibits a non-linear rectifying nature, which is the signature of a Schottky barrier diode.[68,69] The figure portrays a higher current under the

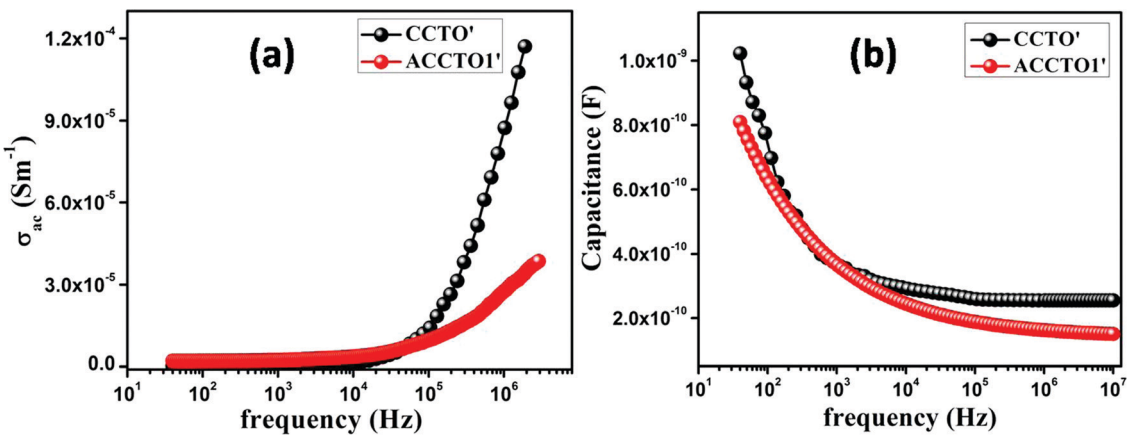

Fig. 7 Dependency of (a) ac conductivity and (b) capacitance on frequency for CCTO′ and ACCTO1′.

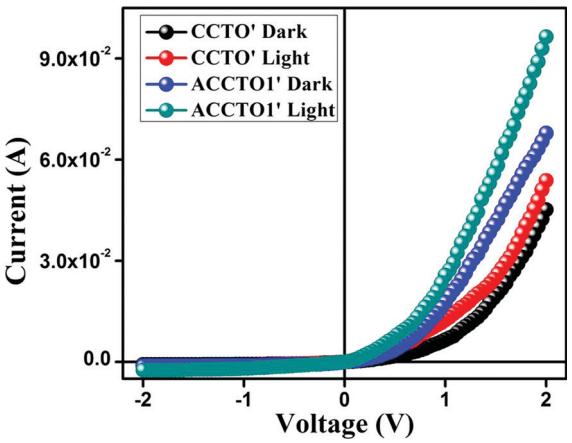

Fig. 8 Current *vs.* voltage graph for CCTO′ and ACCTO1′-based SBDs under dark and light conditions.

photoillumination condition compared to the dark condition. The respective rectification ratios have been calculated to be 36 and 29 respectively for ACCTO1′ and CCTO′ based devices under the dark condition. The same have been calculated as 67 and 56 for ACCTO1′ and CCTO′ based devices, respectively, under the illumination condition. So, the device based on ACCTO1′ shows better rectifying behavior under photo illumination. The measured conductivity for ACCTO1′ based devices is found to be 1.67×10^{-3} S m^{-1} and 2.8×10^{-3} S m^{-1}, respectively, under dark and light conditions, indicating enhanced conductivity under the photo illumination condition. For CCTO′ based devices, the same has been calculated as 0.75×10^{-3} S m^{-1} and 1.72×10^{-3} S m^{-1}, respectively, under dark and light conditions. The photosensitivity of ACCTO1′ and CCTO′ based SBDs has been determined as 1.42 and 1.19.

Fig. 9(a and b) shows dV/d ln(I) *vs.* I and $H(I)$ *vs.* I graphs under dark and light conditions, respectively. The ideality factor (η) has been determined using the intercept values of dV/d ln(I) *vs.* I plot (see Table 2), which is deviated from unity, the ideal value of a diode.[70,71] This may be due to the presence of inhomogeneities in the Schottky barrier height and the existence of interface states, and series resistance at the junction.[72,73]

It is important to note that the value of the ideality factor approaches more the ideal value (closer to 1) after light soaking, which is a signature of less interfacial charge recombination and better homogeneity of the Schottky junctions.[67] It may thus be concluded that our fabricated ACCTO1′ based SBD possesses less carrier recombination at the junction, *i.e.*, better barrier homogeneity under the photoirradiation condition. The value of the barrier height (ϕ_B) for ACCTO1′ based SBDs has been determined from the intercept of H *vs.* I plots and using the ideality factors it has been calculated to be 0.39 eV and 0.30 eV, respectively, under dark and light conditions (Table 2). For CCTO′ based SBDs ϕ_B has been estimated as 0.42 eV and 0.34 eV, respectively, under dark and light conditions (Table 2). So, the potential barrier is reduced when the device is exposed to light. This decrease may be ascribed to the generation of photoinduced charge carriers and their accumulation near the conduction band.[74] The values of series resistance (R_S) have been determined from the slope of dV/d ln(I) *vs.* I and H *vs.* I plots (see Table 2). All the electrical parameters suggest better device performance under the light condition.

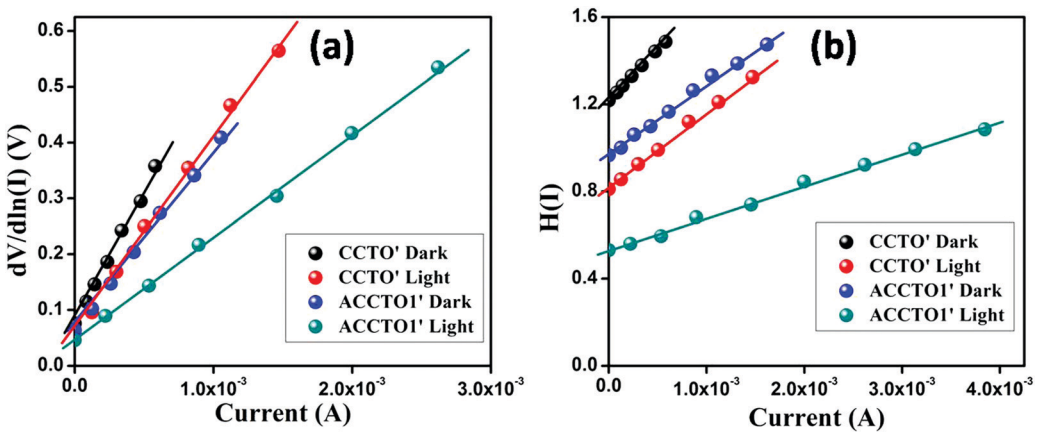

Fig. 9 (a) dV/d ln(I) *vs.* I and (b) $H(I)$ *vs.* I curves for Al/CCTO′/ITO and Al/ACCTO1′/ITO under dark and light conditions.

Table 2 Electrical parameters of ACCTO1′ and CCTO′-based SBDs

Sample	Condition	On/off ratio	Photo-sensitivity	Conductivity $\times 10^{-3}$ (S m^{-1})	Ideality factor	Series resistance (Ω)		Barrier height (eV)
						dV/d ln(I) *vs.* I	$H(I)$ *vs.* I	
ACCTO1′	Dark	36	1.42	1.67	2.46	328	302	0.39
	Light	67		2.8	1.77	185	156	0.30
CCTO′	Dark	29	1.19	0.75	2.89	479	467	0.42
	Light	56		1.72	2.36	352	354	0.34

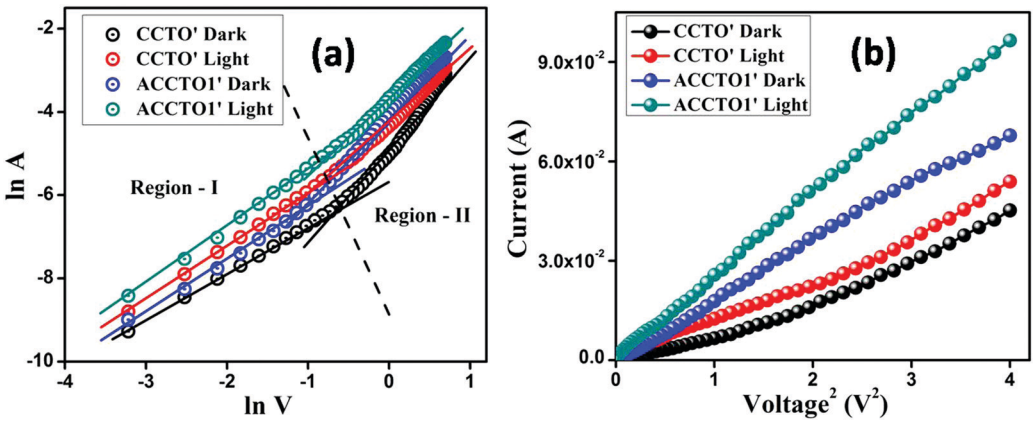

Fig. 10 (a) Current *vs.* voltage (in log scale) and (b) current *vs.* voltage^2 plots for Al/CCTO′/ITO and Al/ACCTO1′/ITO under dark and light conditions.

Table 3 Charge transport parameters of ACCTO1′ and CCTO′-based SBDs

Sample	Condition	$\mu_{eff} \times 10^{-13}$ ($m^2\ V^{-1}\ s^{-1}$)	τ (s)	$\mu_{eff}\tau \times 10^{-13}$ ($m^2\ V^{-1}$)	$D \times 10^{-14}$ ($m^2\ s^{-1}$)	$N_D \times 10^{28}$ ($eV\ m^{-3}$)	$L_D \times 10^{-7}$ (m)
ACCTO1′	Dark	6.57	0.311	2.04	1.64	5.91	1.01
	Light	10.8	0.255	2.75	2.74	6.72	1.17
CCTO′	Dark	3.58	0.571	2.04	0.92	2.45	1.02
	Light	4.47	0.519	2.31	1.15	4.89	1.09

The characteristic *I–V* curves reveal the existence of two regions (see Fig. 10(a)). In Region I, when the value of the slope is ~1, the current follows the relation $I \propto V$ suggesting it to be Ohmic. In Region II, the value of the slope is about 2, meaning $I \propto V^2$, a characteristic feature of a trap free space charge limited current (SCLC).[75–77] If the injected carriers are more than the background carriers, the injected carriers spread and create a space charge field. The effective carrier mobility (μ_{eff}) has been estimated from the higher voltage region of the *I vs.* V^2 plot (Fig. 10(b)) using the Mott–Gurney equation.[75,76] The transit time (τ) of the charge carriers has been estimated from the slope of the SCLC region (Region II).[77] Table 3 represents the diffusion length (L_D), diffusion coefficient (D) and number of generated charge carriers (N_D) near the Fermi level.

All the estimated values of parameters in the SCLC region demonstrate that the charge transport properties of the material are improved after light soaking (see Table 3). The increased diffusion length under illumination reveals that the charge carriers travel more distance before being recombined, which leads to the eventual increase in current displayed by the device under light. The enhanced charge transfer after light soaking is thus expected to pave the way for a very promising future of this material in device application.

Here it may be mentioned that the material polarizability influences the frequency dependent capacitance and the corresponding dielectric property. The dielectric constant of perovskites mainly consists of two parts, one due to electrode polarization at lower frequency and the other due to bulk polarization at higher frequency. The bulk polarization represents the material polarizability which also influences the electrical properties of the material. For our case, the Al doped quadruple perovskite (ACCTO1′) has a higher dielectric constant than its pristine oxide (CCTO′) which suggests greater bulk material polarizability and better electrical property of the doped perovskite.

3.7. TPR studies

The H_2-TPR profile of ACCTO1′ is shown in Fig. 11 along with those of the individual oxides. A comparison of its reduction behavior with those of the pristine oxide phases of the metal components indicates reduction of only Cu-species below 500 °C along with minor contribution from the other metal components. The reducibility pattern of ACCTO1′ is characterized by a slow reduction of copper above 200 °C followed by two distinguishable peaks at 360 °C and 435 °C, the former being more intense than the latter. The shoulder peak near 235 °C is ascribed to the reduction of smaller crystallites. The most intense peak at 360 °C is attributed to the reduction of Cu^{2+}

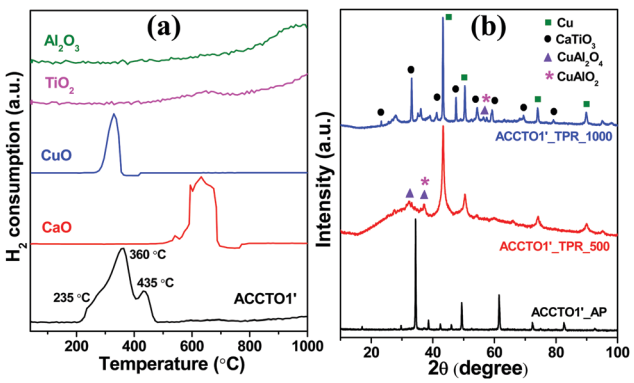

Fig. 11 (a) H_2-TPR profiles of ACCTO1′ along with the pristine oxides and (b) powder XRD patterns of the as-prepared and post TPR samples of ACCTO1′.

associated to the Cu–O–Ti moiety that is followed by the reduction of copper in the Cu–O–Al moiety at a higher temperature of 435 °C.[78] This is also supported by the higher presence of the Cu–O–Ti moiety than the Cu–O–Al moiety (Ti/Al = 3.5).

To gain further insights into the structural transformation subsequent to H_2-reduction, powder XRD phase analysis of the post-TPR sample collected at the end of a complete TPR cycle (ACCTO1′_TPR_1000) and after another cycle of TPR stopped at 500 °C (ACCTO1′_TPR_500) corresponding to the reduction of only Cu-related species has been performed. Both the XRD patterns are compared with that of the parent quadruple perovskite in Fig. 11 that reveals the exclusive presence of metallic Cu (ICDD PDF # 89-2838) subsequent to reduction with complete breakdown of the complex perovskite structure. A thorough analysis of the XRD pattern of the sample reduced up to a lower temperature (ACCTO1′_TPR_500) shows the formation of secondary phases of spinel and delafossite oxides of Cu and Al, which are more prominent in the sample reduced up to a higher temperature (ACCTO1′_TPR_1000). The latter sample is also characterized by the formation of $CaTiO_3$ (ICDD PDF # 65-3287) as the major oxide phase.

The H_2 uptake capacity for ACCTO1′ is found to be 3120 μmol g^{-1} which is less than the calculated value for H_2 consumption (4372 μmol g^{-1}) for complete reduction of copper present in the sample (as per the nominal composition). This discrepancy is essentially due to the formation of $CuAl_2O_4$ (ICDD PDF # 73-1958) and $CuAlO_2$ (ICDD PDF # 77-2494) phases based on the post TPR powder XRD analysis outlined above.

3.8. MSR activities

The methanol reforming behavior of ACCTO1′ is observed to be much higher than that of pure CCTO′ in the whole range of temperatures investigated (see Fig. 12). ACCTO1′ shows an initially low methanol conversion up to ~230 °C that increases by about 45% for an increase of temperature by ~20 °C, when the pristine oxide CCTO′ remains inactive. The methanol conversion recorded over ACCTO1′ reaches up to 82% in the temperature range of 245–300 °C, beyond which the conversion increases only marginally to 85%. The CO selectivity is low up to 290 °C, and remains little higher, higher than that obtained for CCTO′, afterwards. So, doping of Al in CCTO has the beneficial effect of lowering the methanol conversion temperature considerably, but with a marginally higher CO selectivity.

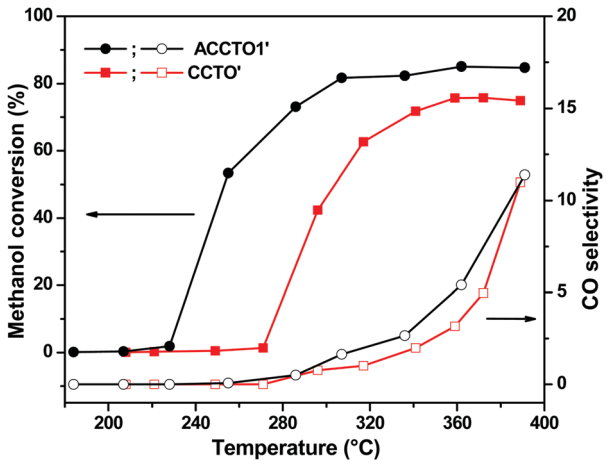

Fig. 12 Methanol conversion and CO selectivity of ACCTO1′ and its pristine oxide CCTO′ at a GHSV of 33 000 h^{-1}.

In this regard, it can be mentioned that there is no literature report till date on the MSR activity of Al-containing perovskite materials barring our recent study on pure and Mn-doped CCTO.[18] Not only MSR catalysts, any Al-containing perovskite material is hardly to be found which is active towards these types of catalytic reactions.[79] There are also a very limited number of literature reports that are focused on the usefulness of normal perovskite based materials for MSR reaction.[80,81] Mukai *et al.* have reported the synthesis of the $Ni/La_{0.7}Sr_{0.3}AlO_{3-\delta}$ catalyst and have studied steam reforming of toluene using the catalyst.[79] Natile *et al.* have found that the MSR activity is good over the $La_{0.6}Sr_{0.4}Co_{1-y}Fe_yO_{3-\delta}$ perovskite with a standard H_2 selectivity.[80] They have recorded a methanol conversion of 50% at 367 °C for the y = 0.2 sample that is attributed to the enhancement of the Co/Fe atomic ratio. They have also shown that introduction of a prereduction treatment has only a minor role in the activity. MSR catalysts have also been derived *via* reductive pretreatment of the perovskite-type $LaCo_{1-x-y}Pd_xZn_yO_{3\pm\delta}$ oxide at two different temperatures to study the MSR activity under different reducible environments.[81] The CO_2 selectivity of the catalysts is found to be sensitive to their composition and the degree of Pd–Zn alloy formation. We can thus conclude that the Al-doped CCTO quadruple perovskite, which does not require any pretreatment, exhibits an admirable methanol conversion behavior with low CO selectivity in MSR as compared with the pure CCTO as well as the other normal perovskite materials reported in the literature.

4. Conclusions

The present investigation has suggested that Al-doped $CaCu_3Ti_4O_{12}$ is a highly potential multifunctional material. It can be easily synthesized at moderately lower temperature by the modified citrate combustion route in nano size. The material is crystallized in the $Im\bar{3}$ cubic space group. The XPS analysis has confirmed the nominal cationic composition and valence state within the probe depth of the sample surface. The substitution of non-magnetic cations does not affect the low temperature antiferromagnetic ordering in $CaCu_3Ti_4O_{12}$. The high dielectric constant is ascribed to the grain boundary effects. Most importantly the Al-doped $CaCu_3Ti_4O_{12}$ is revealed to show a better performance as a Schottky barrier diode compared to the undoped $CaCu_3Ti_4O_{12}$, which is used in optoelectronic devices. Finally, the large surface area of the nanodimensional material as well as the square planar coordination of Cu^{2+} ions provides a better opportunity for the material to act as a potential catalyst. The Al-doped sample has shown much improved and efficient performance in methanol steam reforming in comparison to the pristine oxide. This result has underscored the potential applicability of the quadruple

perovskite material in energy related issues. We believe that our findings would be of interest to the materials community searching for multifunctional materials and it can also motivate researchers for theoretical calculations.

Conflicts of interest

There are no conflicts to declare.

Acknowledgements

Financial support from the Science and Engineering Research Board (SERB), Government of India, through the grant EMR/2016/001811 to A. Gayen, EMR/2016/000083 to Md. M. Seikh and EMR/2016/005387 to Partha P. Ray is gratefully acknowledged. The UGC research fellowship to K. Pal and the DST Special Grant to the Department of Chemistry in the International Year of Chemistry 2011 and the UPE II Grant to Jadavpur University are also highly acknowledged.

References

1 M. A. Subramanian, D. Li, N. Duan, B. A. Reisner and A. W. Sleight, *J. Solid State Chem.*, 2000, **151**, 323–325.
2 A. P. Ramirez, M. A. Subramanian, M. Gardel, G. Blumberg, D. Li, T. Vogt and S. M. Shapiro, *Solid State Commun.*, 2000, **115**, 217–220.
3 C. C. Homes, T. Vogt, S. M. Shapiro, S. Wakimoto and A. P. Ramirez, *Science*, 2001, **293**, 673–676.
4 C. C. Homes, T. Vogt, S. M. Shapiro, S. Wakimoto, M. A. Subramanian and A. P. Ramirez, *Phys. Rev. B: Condens. Matter Mater. Phys.*, 2003, **67**, 092106.
5 A. Deschanvres, B. Raveau and F. Tollemer, *Bull. Soc. Chim. Fr.*, 1967, **11**, 4077.
6 L. He, J. B. Neaton, M. H. Cohen, D. Vanderbilt and C. C. Homes, *Phys. Rev. B: Condens. Matter Mater. Phys.*, 2002, **65**, 214112.
7 D. C. Sinclair, T. B. Adams, F. D. Morrison and A. R. West, *Appl. Phys. Lett.*, 2002, **80**, 2153–2155.
8 T. B. Adams, D. C. Sinclair and A. R. West, *Adv. Mater.*, 2002, **14**, 1321–1323.
9 M. H. Cohen, J. B. Neaton, L. He and D. Vanderbilt, *J. Appl. Phys.*, 2003, **94**, 3299–3306.
10 A. Collomb, D. Samaras, B. Bochu, J. Chenavas, M. N. Deschizeaux, G. Fillion, J. C. Joubert and M. Marezio, *Physica B*, 1977, **86–88**, 927–928.
11 Z. Zeng, M. Greenblatt, M. A. Subramanian and M. Croft, *Phys. Rev. Lett.*, 1999, **82**, 3164–3167.
12 S. Y. Chung, I. D. Kim and S. J. L. Kang, *Nat. Mater.*, 2004, **3**, 774–778.
13 P. Leret, J. F. Fernandez, J. de Frutos and D. Fernández-Hevia, *J. Eur. Ceram. Soc.*, 2007, **27**, 3901–3905.
14 S. Y. Chung, J. H. Choi and J. K. Choi, *Appl. Phys. Lett.*, 2007, **91**, 091912.
15 J. H. Clark, M. S. Dyer, R. G. Palgrave, C. P. Ireland, J. R. Darwent, J. B. Claridge and M. J. Rosseinsky, *J. Am. Chem. Soc.*, 2011, **133**, 1016–1032.
16 D. R. Clarke, *J. Am. Ceram. Soc.*, 1999, **82**, 485–502.
17 H. S. Kushwaha, N. A. Madhar, B. Ilahi, P. Thomas, A. Halder and R. Vaish, *Sci. Rep.*, 2016, **6**, 8557.
18 K. Pal, A. Dey, P. P. Ray, N. E. Mordvinova, O. I. Lebedev, T. K. Mandal, M. M. Seikh and A. Gayen, *ChemistrySelect*, 2018, **3**, 1076–1087.
19 J. Liu, R. W. Smith and W. N. Mei, *Chem. Mater.*, 2007, **19**, 6020–6024.
20 J. Liu, Y. Sui, C. Duan, W. Mei, R. W. Smith and J. R. Hardy, *Chem. Mater.*, 2006, **18**, 3878–3882.
21 A. Sen, U. N. Maiti, R. Thapa and K. K. Chattopadhyay, *J. Alloys Compd.*, 2010, **506**, 853–857.
22 A. K. Rai, K. D. Mandal, D. Kumar and O. Parkash, *J. Alloys Compd.*, 2010, **491**, 507–512.
23 L. Ren, L. Yang, C. Xu, X. Zhao and R. Liao, *J. Alloys Compd.*, 2018, **768**, 652–658.
24 J. Wang, Z. Lu, T. Deng, C. Zhong and Z. Chen, *J. Eur. Ceram. Soc.*, 2018, **38**, 3505–3511.
25 S. Said, S. Didry, M. E. Amrani, C. Autret-lambert and A. Megriche, *J. Alloys Compd.*, 2018, **765**, 927–935.
26 P. Y. Raval, P. R. Pansara, A. R. Makadiya, N. H. Vasoya, S. N. Dolia and K. B. Modi, *Ceram. Int.*, 2018, **44**, 17667–17674.
27 S. W. Choi, S. H. Hong and Y. M. Kim, *J. Am. Ceram. Soc.*, 2007, **90**, 4009–4011.
28 R. Jia, X. Zhao, J. Li and X. Tang, *Mater. Sci. Eng., B*, 2014, **185**, 79–85.
29 G. Du, F. Wei, W. Li and N. Chen, *J. Eur. Ceram. Soc.*, 2017, **37**, 4653–4659.
30 J. Boonlakhorn, P. Kidkhunthod, N. Chanlek and P. Thongbai, *J. Eur. Ceram. Soc.*, 2018, **38**, 137–143.
31 S. D. Almeida-Didry, M. M. Nomel, C. Autret, C. Honstettre, A. Lucas, F. Pacreau and F. Gervais, *J. Eur. Ceram. Soc.*, 2018, **38**, 3182–3187.
32 D. R. Palo, R. A. Dagle and J. D. Holladay, *Chem. Rev.*, 2007, **107**, 3992–4021.
33 J. Li, M. A. Subramanian, H. D. Rosenfeld, C. Y. Jones, B. H. Toby and A. W. Sleight, *Chem. Mater.*, 2004, **16**, 5223–5225.
34 A. L. Patterson, *Phys. Rev.*, 1939, **56**, 978–982.
35 A. Goktas, A. Tumbul, Z. Aba and M. Durgun, *Thin Solid Films*, 2019, **680**, 20–30.
36 A. Goktas, A. Tumbul and F. Aslan, *J. Sol-Gel Sci. Technol.*, 2019, **90**, 487–497.
37 T. Ebina, T. Ewasaki, A. Chatterjee, M. Katagiri and G. D. Stucky, *J. Phys. Chem. B*, 1997, **101**, 1125–1129.
38 G. Manjunath, R. V. Vardhan, A. Salian, R. Jagannatha, M. Kedia and S. Mandal, *Bull. Mater. Sci.*, 2018, **41**, 126.
39 R. V. Lakshmi, P. Bera and C. Anandan, *RSC Adv.*, 2016, **6**, 36345–36355.
40 R. Bechara, A. Aboukaïs and J.-P. Bonnelle, *J. Chem. Soc., Faraday Trans.*, 1993, **89**, 1257–1262.
41 F. Li, L. Zhang, D. G. Evans and X. Duan, *Colloids Surf., A*, 2004, **244**, 169–177.

42 C. Xu, S. Li, Y. Zhang, Y. Li, J. Zhou and G. Qin, *Int. J. Hydrogen Energy*, 2019, **44**, 4156–4166.
43 C. Elmi, S. Guggenheim and R. Gieré, *Clays Clay Miner.*, 2016, **64**, 537–551.
44 T. L. Barr, S. Seal, K. Wozniak and J. Klinowski, *J. Chem. Soc., Faraday Trans.*, 1997, **93**, 181–186.
45 J.-C. Dupin, D. Gonbeau, P. Vinatier and A. Levasseur, *Phys. Chem. Chem. Phys.*, 2000, **2**, 1319–1324.
46 S. Krohns, J. Lu, P. Lunkennheimer, F. Gervais, F. Porcher and A. Loidl, *Eur. Phys. J. B*, 2009, **72**, 173–182.
47 A. Haque, D. Ghosh, U. Dutta, A. Shukla, A. Gayen, P. Mahata, A. K. Kundu and M. M. Seikh, *J. Magn. Magn. Mater.*, 2020, **494**, 165847.
48 F. Mikailzade, F. Onal, M. Maksutoglu, M. Zarbali and A. Goktas, *J. Supercond. Novel Magn.*, 2018, **31**, 4141–4145.
49 H. Gencer, M. Gunes, A. Goktas, Y. Babur, H. I. Mutlu and S. Atalay, *J. Alloys Compd.*, 2008, **465**, 20–23.
50 C. Chen, W. Gao, Z. Qin, W. Hu and M. Qu, *J. Appl. Phys.*, 1991, **70**, 6277–6279.
51 M. M. Seikh, V. Caignaert, V. Pralong and B. Raveau, *Appl. Phys. Lett.*, 2013, **103**, 082401.
52 M. M. Seikh, V. Caignaert, A. Sundaresan, C. De and B. Raveau, *J. Mater. Chem. C*, 2014, **2**, 6061–6067.
53 C. Lacroix, *J. Phys. C: Solid State Phys.*, 1980, **13**, 5125–5136.
54 *Impedance spectroscopy*, ed. J. R. Macdonald, Wiley, New York, 1987.
55 C. P. Symth, *Dielectric behaviour and structure*, McGraw-Hill, New York, 1955.
56 V. L. Rao, T. Shekharam, T. M. Kumar and M. Nagabhushanam, *Mater. Chem. Phys.*, 2015, **159**, 83–92.
57 P. S. Archana, A. Gupta, M. M. Yusoff and R. Jose, *Phys. Chem. Chem. Phys.*, 2014, **16**, 7448–7454.
58 S. K. Barik, R. N. P. Choudhary and P. K. Mahapatra, *Appl. Phys. A: Mater. Sci. Process.*, 2007, **88**, 217–222.
59 H. M. Chenari, A. Hassanzadeh, M. Golzan, H. Sedghi and M. Talebian, *Curr. Appl. Phys.*, 2011, **11**, 409–413.
60 G. B. Kumar and S. Buddhudu, *Ceram. Int.*, 2010, **36**, 1857–1861.
61 J. C. Anderson, *Dielectrics*, Chapman & Hall, London, 1964.
62 A. Gautam, P. Uniyal, K. L. Yadav and V. S. Rangra, *J. Phys. Chem. Solids*, 2012, **73**, 188–192.
63 A. K. Jonscher, *J. Phys. D: Appl. Phys.*, 1999, **32**, R57–R70.
64 K. Funke, *J. Non-Cryst. Solids*, 1994, **172**, 1215–1221.
65 I. Rivera, A. Kumar, F. Mendoza and R. Katiyar, *Physica B*, 2008, **403**, 2423–2430.
66 S. Saha, S. Chanda, A. Dutta and T. P. Sinha, *Mater. Res. Bull.*, 2013, **48**, 4917–4923.
67 A. Dey, A. Layek, A. Roychowdhury, M. Das, J. Datta, S. Middya, D. Das and P. P. Ray, *RSC Adv.*, 2015, **5**, 36560–36567.
68 A. A. Felix, J. L. M. Rupp, J. A. Varela and M. O. Orlandi, *J. Appl. Phys.*, 2012, **112**, 054512.
69 R. Bodeux, M. Gervais, J. Wolfman and F. Gervais, *Appl. Phys. A: Mater. Sci. Process.*, 2014, **116**, 2001–2006.
70 E. H. Rhoderick, *Metal semiconductors contacts*, Oxford University Press, Oxford, 1978.
71 S. K. Cheung and N. W. Cheung, *Appl. Phys. Lett.*, 1986, **49**, 85–87.
72 R. K. Gupta and F. Yakuphanoglu, *Sol. Energy*, 2012, **86**, 1539–1545.
73 X. Miao, S. Tongay, M. K. Petterson, K. Berke, A. G. Rinzler, B. R. Appleton and A. F. Hebard, *Nano Lett.*, 2012, **12**, 2745–2750.
74 A. Dey, S. Middya, R. Jana, M. Das, J. Datta, A. Layek and P. P. Ray, *J. Mater. Sci.: Mater. Electron.*, 2016, **27**, 6325–6335.
75 P. W. M. Blom, M. J. M. de Jong and M. G. van Munster, *Phys. Rev. B: Condens. Matter Mater. Phys.*, 1997, **55**, R656–R659.
76 K. Pal, R. Jana, A. Dey, P. P. Ray, M. M. Seikh and A. Gayen, *Chem. Phys. Lett.*, 2018, **699**, 229–233.
77 K. Pal, R. Jana, A. Dey, P. P. Ray, M. M. Seikh and A. Gayen, *Chem. Phys. Lett.*, 2018, **709**, 110–115.
78 K. Samson, A. Zelazny, R. Grabowski, M. R. Mikolajczyk, M. Sliwa, K. Pamin, A. Kornas and M. Lachowska, *Res. Chem. Intermed.*, 2015, **41**, 9295–9306.
79 D. Mukai, Y. Murai, T. Higo, S. Tochiya, T. Hashimoto, Y. Sugiura and Y. Sekine, *Appl. Catal., A*, 2013, **466**, 190–197.
80 M. M. Natile, F. Poletto, A. Galenda, A. Glisenti, T. Montini, L. D. Rogatis and P. Fornasiero, *Chem. Mater.*, 2008, **20**, 2314–2327.
81 J. Kuc, M. Neumann, M. Armbruster, S. Yoon, Y. Zhang, R. Erni, A. Weidenkaffe and S. K. Matam, *Catal. Sci. Technol.*, 2016, **6**, 1455–1468.